Journal of Alloys and Compounds 503 (2010) 31–39

Contents lists available at ScienceDirect

Journal of Alloys and Compounds

journal homepage: www.elsevier.com/locate/jallcom

Numerical and experimental investigation of microporosity formation in a ternary Al–Cu–Si alloy

Ivaldo L. Ferreira [a], Jefferson F.C. Lins [a], Daniel J. Moutinho [b], Laércio G. Gomes [b], Amauri Garcia [c,*]

[a] Department of Mechanical Engineering, Fluminense Federal University, Av. dos Trabalhadores, 420 – 27255-125 Volta Redonda, RJ, Brazil
[b] Federal Institute of Education, Science and Technology – IFPA, PO Box 479 – 66093-020 Belém, PA, Brazil
[c] Department of Materials Engineering, University of Campinas – UNICAMP, PO Box 6122, 13083-860 Campinas, SP, Brazil

ARTICLE INFO

Article history:
Received 16 March 2010
Received in revised form 24 April 2010
Accepted 29 April 2010
Available online 6 May 2010

Keywords:
Metals and alloys
Composition fluctuations
Thermal analysis
Computer simulations

ABSTRACT

Macrosegregation and porosity formation are investigated by both a numerical model and transient directional solidification experiments. The macrosegregation pattern, and the theoretical and apparent densities are presented as a function of the casting length. X-ray fluorescence spectrometry was used to determine the experimental macrosegregation profiles. The measurement of microporosity was performed by a pyknometry procedure. The local composition along an Al–6 wt%Cu–1 wt%Si casting length is used as an input parameter for simulations of microporosity evolution. The results show that the addition of 1 wt% silicon to the Al–Cu alloy composition increases significantly the volumetric fraction of pores as compared with the corresponding porosity exhibited by an Al–6 wt%Cu alloy casting. It is also shown that the use of a carbon steel chill mold induced an abnormal increase in the fraction of pores close to the casting cooled surface which was caused by a higher Fe concentration provoked by the diffusive flux of iron from the chill.

1. Introduction

Microporosity formation during casting and solidification of aluminum alloys often causes severe problems in the manufacture of quality products. The process parameters during transient solidification affect the microstructural development of the alloy and consequently the final engineering performance of the casting. The dendrite arm spacings; segregation patterns; nature, size, distribution and morphology of precipitates as well as porosity, all affect final mechancial properties. Porosity has also a deleterious effect on the machinability and surface properties of aluminum castings [1–4].

Porosity in aluminum castings is normally a result of two phenomena: insufficient feeding and/or hydrogen precipitation during solidification. Because of its low solubility, the atomic hydrogen rejected by the solid phase enriches continuously the melt around the solid phase already formed. When the liquid reaches its critical hydrogen concentration, molecular hydrogen bubbles begin to form, and depending on the local hydrogen content, partial pressure and gas diffusivity, bubbles evolve either to grow or to dissolve back into the melt [5].

To prevent shrinkage from appearing as porosity, material movement, i.e., feeding, has to occur through the alloy mushy zone. Piwonka et al. have reported that porosity forms because of the impossibility of the liquid to fill up the regions where the pores are forming [6]. In alloys with large solidification ranges, depending on the local solid fraction, five distinct feeding mechanisms may be envisaged: liquid feeding, mass feeding, interdendritic feeding, burst feeding and solid feeding. A detailed description of these mechanisms can be found in the literature [7–9]. Liquid metal feeding occurs above the liquidus temperature when the liquid is free to move to the point of metal shrinkage; mass feeding occurs when solid crystals first form in the liquid. In mass feeding the dendritic crystals are carried along with the liquid, as in the slurry. These dendrites initially grows independently of each other, but impinge and form an interconnected solid network at the dendritic coherency point, usually between 10% and 50% solid [10]. After coherency the material starts to develop strength and the resistance to material movement increases drastically. Interdendritic feeding occurs after the coherency point. Liquid travels through tortuous, narrow interdendritic channels. In this context, is important to know the solid fraction at the coherency point, as it determines just how difficult it will be to feed porosity. The coherency point depends on grain size [11], alloy composition, and cooling rate [12]. Burst feeding occurs when the strength of the dendritic network is insufficient to resist the increasing pressure induced by continuous solidification shrinkage [7,8]. Solid feeding denotes the feeding of solid material by deformation, i.e., the stress on the dendrites increase and the network may collapse, giving rise to transport of solid fragments and liquid. Alloy composition has a fundamental role on

* Corresponding author. Tel.: +55 19 35213320; fax: +55 19 32893722.
E-mail address: amaurig@fem.unicamp.br (A. Garcia).

0925-8388/$ – see front matter © 2010 Elsevier B.V. All rights reserved.
doi:10.1016/j.jallcom.2010.04.244

the feedability during solidification. The narrowing interdendritic fluid paths may become blocked by inclusions or growing intermetallic particles in the melt stream. Iron, for instance, exists as a commom impurity element in aluminum alloys. For Al–Si alloys the main microstructural consequence is the formation of Al_5FeSi intermetallic particles, which affect porosity levels in such alloys. Dinnis et al. developed an experimental program to analyse the effect of iron concentrations on porosity levels of Al–Si–Cu foundry alloys [13].

Studies on transient solidification of ternary alloys related to microstructural parameters, solidification modelling, solute segregation and porosity formation are relatively scarce in the literature [14–17]. The main difficulty is related to the determination of the ternary solidification path and the intermediate phases reactions, which has to be coupled with the model. Macrosegregation is critical in determining porosity along the casting length due to the resultant impact upon the local density. Ferreira et al. proposed a numerical scheme to simulate the transient solidification of an Al–Cu–Si alloy for the analysis of inverse segregation, considering the absence of intermediate phases and reactions [18]. In a recent study Ferreira et al. proposed a numerical approach taking into account secondary phases transformations, which permits the prediction of macrosegregation profiles during the transient directional solidification of ternary alloys [19]. Tsoukalas applied a genetic algorithm method to determine the optimum process parameters in real industry environmment leading to minimum porosity in Al–9.5 wt%Si–3 wt%Cu die castings [20].

In this paper, a model considering intermediate phases and reactions is used to simulate the macrosegregation profile and microporosity formation along the length of a ternary Al–6 wt%Cu–1 wt%Si casting. The simulated segregation pattern is checked against experimentally measured values and is used for theoretical calculations of local density as a function of the solute content along the casting length. The local composition is used as an input parameter for simulations of microporosity evolution, which is compared with the experimenal pores distribution. The effect of a higher Fe concentration on regions close to the casting surface (which have been contamined by the steel chill mold) on local porosity formation is also examined.

2. Numerical model

2.1. Macrosegregation

The numerical model approach used to simulate the macrosegregation profile during solidification is based on a model previously proposed by Voller [15,16] and modified by Boeira et al. [21,22] to deal with microporosity formation. For times $t < 0$, the molten alloy is at the nominal concentration C_0, and contained in the insulated two-dimensional mold defined by $0 < x < X_b$ and $0 < y < Y_b$.

In the development of the numerical solution (thermal and solutal coupled fields), the following assumptions were assumed:

(i) the region is two-dimensional, defined by $0 < x < X_b$ and $0 < y < Y_b$, where Y_b is a point far removed from the segregation region;
(ii) the segregation region does not remain free of porosity;
(iii) the solid phase is stationary, i.e., once formed has zero velocity;
(iv) due to the rapid nature of heat and liquid mass diffusion, the liquid concentration C_l, the temperature T, the liquid density ρ_l and the liquid velocity u_l are assumed to be constants in a representative elemental volume [14];
(v) the partition coefficient k_0 and the liquidus slope m_L, may either assumed to be constants or variables and read from the ThermoCalc databases;
(vi) equilibrium conditions exist at the solid/liquid interface, i.e., at this interface we have:

$$T = f(C_L^{Cu}, C_L^{Si}) \quad \text{and} \quad C_S^* = k_0 C_L \tag{1}$$

where T is the equilibrium temperature, C is the concentration, and C_S^* is the interface solid concentration;
(vii) the specific heats, c_S, c_L, c_{eutS}, c_{eutL}, the thermal conductivities, k_S, k_L, k_{eutS}, k_{eutL} and the densities ρ_S, ρ_L, ρ_{eutS}, ρ_{eutL}, are constants within each phase, but discontinuous between the solid and liquid phases. Latent heats of phase formation, ΔH_1, ΔH_2 and ΔH_{eut} are taken as the difference between phase enthalpies;
(viii) the metal/mold thermal resistance varies with time, and is incorporated in a global heat-transfer coefficient defined as h_g.

The ThermoCalc software has been used to generate equilibrium phase diagrams. Through the ThermoCalc TCAPI interface for Intel Visual Fortran, it is possible to recall and to record data from ThermoCalc prior to any numerical simulation of multicomponent alloys, a procedure that provides more accurate phase diagram data. The pseudo-binary phase diagrams as a function of Cu, Si and H concentrations and the phase diagram surfaces for the hypoeutectic Al–Cu–Si system obtained by this routine are presented in Figs. 1 and 2, respectively.

Considering the assumptions previously presented, the mixture equations for multicomponent solidification are the following:

- Mass

$$\frac{\partial \rho}{\partial t} + \nabla \cdot (\rho \boldsymbol{V}) = 0 \tag{2}$$

- Momentum x

$$\frac{\partial(\rho u)}{\partial t} + \nabla \cdot (\rho \boldsymbol{V} u) + \frac{\partial P}{\partial x} = \nabla \cdot \left(\mu_L \frac{\rho}{\rho_L} \nabla u \right) - \frac{\mu_L}{K_X}(u - u_S) + \rho g_X \tag{3}$$

- Momentum y

$$\frac{\partial(\rho v)}{\partial t} + \nabla \cdot (\rho \boldsymbol{V} v) + \frac{\partial P}{\partial y} = \nabla \cdot \left(\mu_L \frac{\rho}{\rho_L} \nabla v \right) - \frac{\mu_L}{K_Y}(v - v_S) + \rho g_Y \tag{4}$$

g_X and g_Y, depending on the number of species, can be written as

$$g_{X,Y} = g_0 \sum_{\mathrm{Cu,Si}} [\beta_S^i (C_l^i - C_{l,0}^i) + \beta_T^i (T - T_0)] \tag{5}$$

and, in our current setup, $g_X = 0$.

- Energy

$$\frac{\partial}{\partial t}(\rho c_P T) + \nabla \cdot (\rho c_P \boldsymbol{V} T) = \nabla \cdot (k \nabla T) - \frac{\partial}{\partial t}(\Delta H_f \rho_S g_S) \tag{6}$$

- Species

$$\frac{\partial}{\partial t}(\rho C^{Cu}) + \nabla \cdot (\rho \boldsymbol{V} C^{Cu}) = \nabla \cdot (\rho D^{Cu} \nabla C^{Cu}) + \nabla \cdot [\rho D^{Cu} \nabla (C_l^{Cu} - C^{Cu})] - \nabla \cdot [\rho (\boldsymbol{V} - \boldsymbol{V}_S)(C_l^{Cu} - C^{Cu})] \tag{7a}$$

$$\frac{\partial}{\partial t}(\rho C^{Si}) + \nabla \cdot (\rho \boldsymbol{V} C^{Si}) = \nabla \cdot (\rho D^{Si} \nabla C^{Si}) + \nabla \cdot [\rho D^{Si} \nabla (C_l^{Si} - C^{Si})] - \nabla \cdot [\rho (\boldsymbol{V} - \boldsymbol{V}_S)(C_l^{Si} - C^{Si})] \tag{7b}$$

- Mixture density

$$\rho = \int_0^{1-g_l} \rho_S \, d\alpha + g_l \rho_l \tag{8}$$

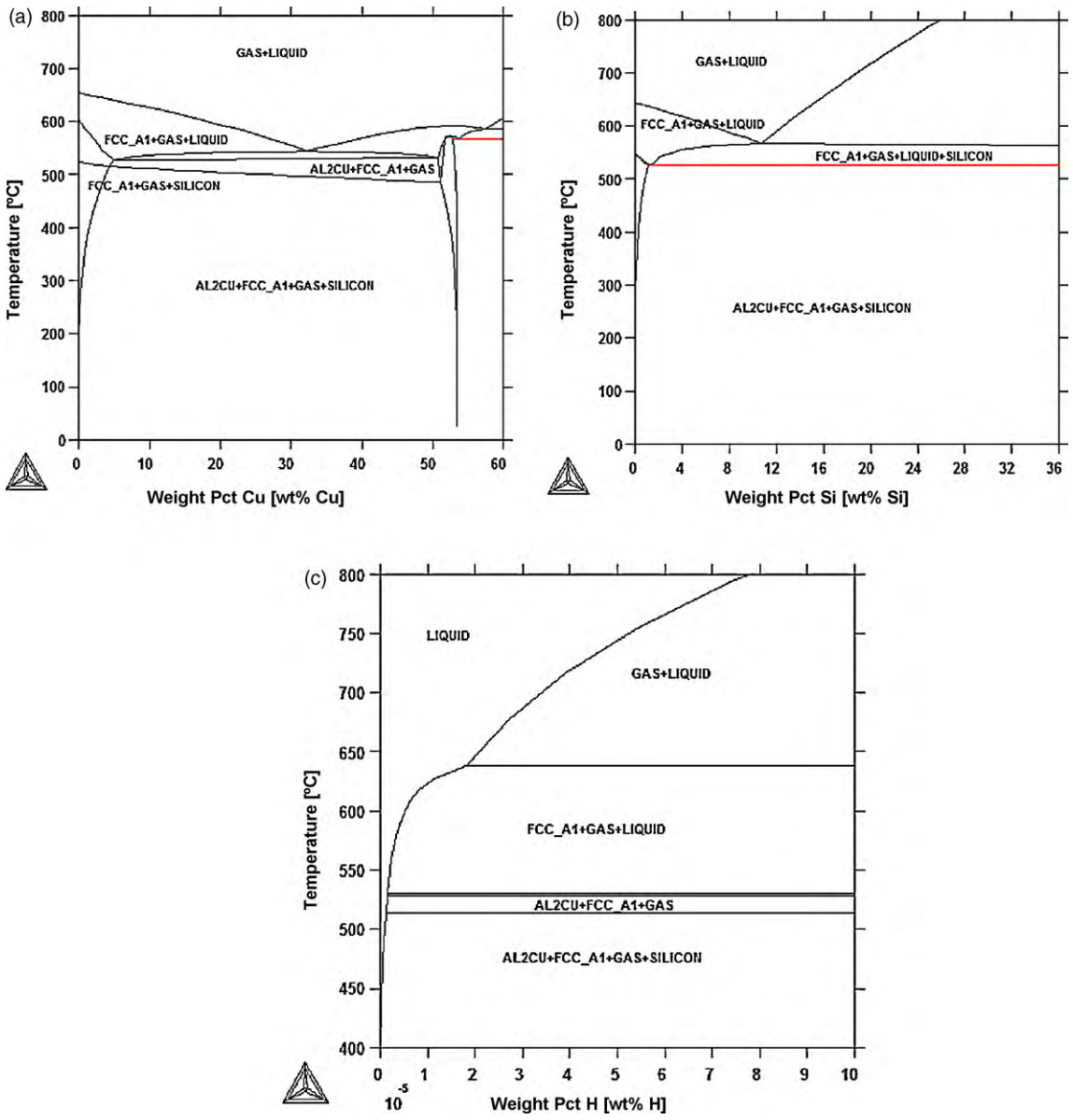

Fig. 1. Al–Cu–Si–H system. Pseudo-binary phase diagram as a function of Cu (a), Si (b) and hydrogen (c).

- Mixture solute density

$$\rho C = \int_0^{1-g_l} \rho_S C_S \, d\alpha + g_l \rho_l C_l \tag{9}$$

and the variables are defined as

$$\mathbf{V} = g_l \mathbf{V}_l + g_S \mathbf{V}_S \tag{10}$$

$$g = g_l + g_S + g_g \tag{11}$$

$$f = f_l + f_S + f_g \tag{12}$$

$$k = k_S g_S + k_l g_l + k_g g_g \tag{13}$$

$$\rho = \rho_S g_S + \rho_l g_l + \rho_g g_g \tag{14}$$

$$f_S = \frac{g_S \rho_S}{\rho}, \qquad f_l = \frac{g_l \rho_l}{\rho}, \qquad f_g = \frac{g_g \rho_g}{\rho} \tag{15}$$

$$c_P = c_{PS} f_S + c_{Pl} f_l + c_{Pg} f_g \tag{16}$$

$$D^{Cu} = D_S^{Cu} f_S + D_l^{Cu} f_l \tag{17}$$

$$D^{Si} = D_S^{Si} f_S + D_l^{Si} f_l \tag{18}$$

where g_l, g_S and g_g are the liquid, solid and gas volume fractions, f_l, f_S and f_g are the liquid, solid and gas mass fractions, u and v are the volume averaged fluid velocities, D_l and D_S are the liquid and solid mass-diffusion coefficients, k_l, k_S and k_g are the liquid, solid and gas thermal conductivities, c_{Pl}, c_{PS} and c_{Pg} are the liquid, solid and gas heat capacities, and finally, ρ_l, ρ_S and ρ_g are the liquid, solid and gas densities.

A micro-scale model is invoked to extract nodal values of liquid concentration C_l from each solute density field $(\rho C)^\zeta$, where ζ = Cu, Si. The key variable in this calculation is the nodal liquid fraction calculated in the previous step. A detailed discussion was previously presented by Voller [15], in which the application of the back diffusion model proposed by Wang and Beckermann [17] is suggested.

The species local liquid concentrations are given by

$$[C_L^{Cu}]_P = \frac{[\rho C]_P^{Cu} - [\rho C]_P^{Cu,old} + [\rho_L g_P^{old} + \beta^{Cu}\rho_S(1 - g_P^{old})k_0^{Cu}][C_L^{Cu}]_P^{old}}{\rho_L g_P^{n+1} + \beta^{Cu}\rho_S(1 - g_P^{n+1})k_0^{Cu} + (1 - \beta^{Cu})\rho_S k_0^{Cu}(g_P^{old} - g_P^{n+1})} \tag{19a}$$

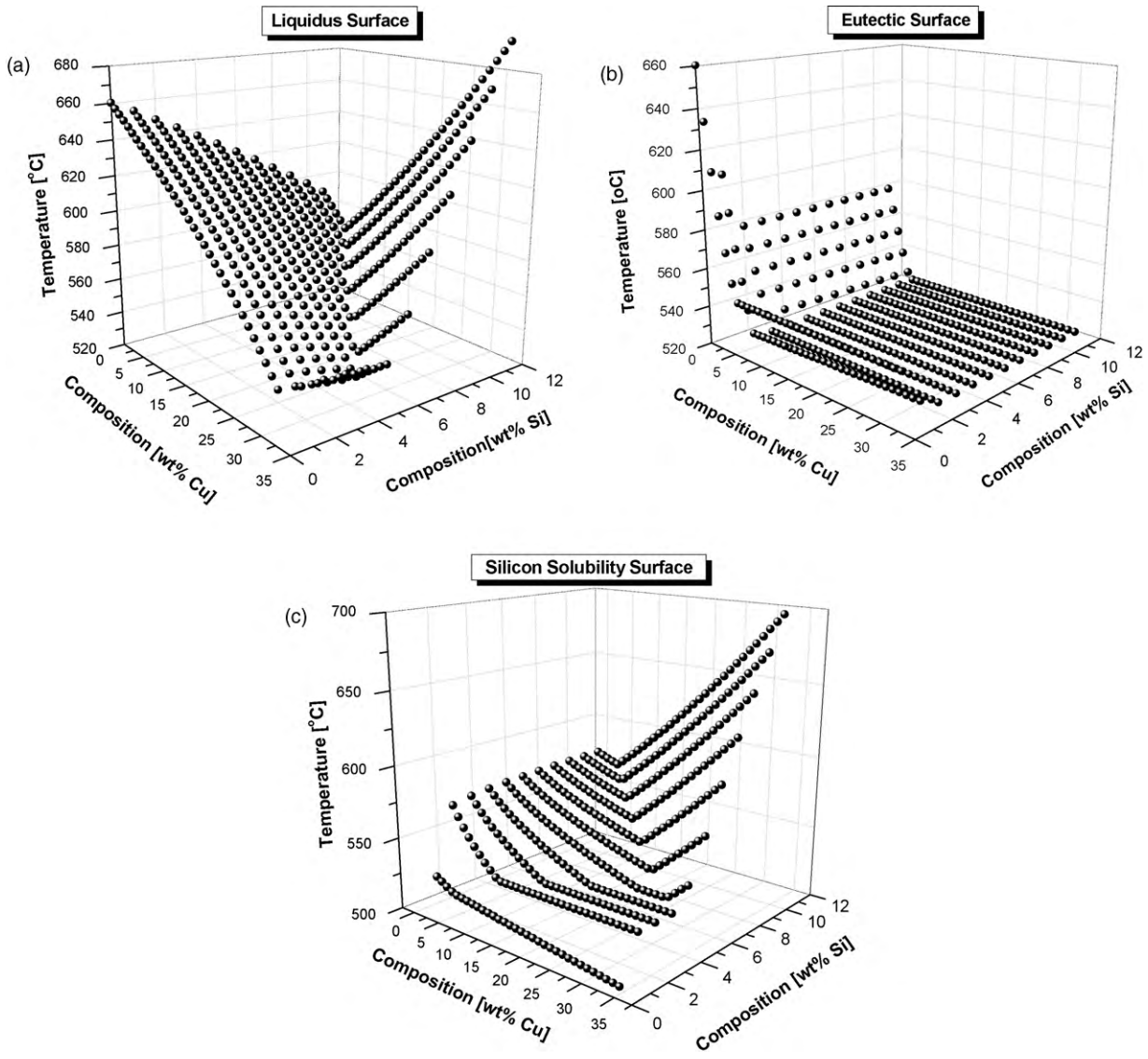

Fig. 2. Al–Cu–Si–H system. Phase diagram surfaces: liquidus surface (a), eutectic surface (b) and silicon solubility surface (c).

$$[C_L^{\mathrm{Si}}]_P = \frac{[\rho C]_P^{\mathrm{Si}} - [\rho C]_P^{\mathrm{Si},old} + [\rho_L g_P^{old} + \beta^{\mathrm{Si}}\rho_S(1-g_P^{old})k_0^{\mathrm{Si}}][C_L^{\mathrm{Si}}]_P^{old}}{\rho_L g_P^{n+1} + \beta^{\mathrm{Si}}\rho_S(1-g_P^{n+1})k_0^{\mathrm{Si}} + (1-\beta^j)\rho_S k_0^{\mathrm{Si}}(g_P^{old} - g_P^{n+1})} \tag{19b}$$

2.2. Microporosity formation

The present porosity model is based on a previous formulation by Kuznetsov and Xiong [23], where the porosity formation has been separated in two distinct stages: nucleation and growth. They adopted as the nucleation condition, the moment in which the mean hydrogen contents in the liquid and in the solid phases (C_{L+S}^{H}) are less than that of the initial hydrogen concentration in the molten alloy (C_0^{H}). The condition of pore nucleation can be expressed as

$$C_{L+S}^{\mathrm{H}} < C_0^{\mathrm{H}} \tag{20}$$

Though the initial hydrogen concentration in the melt can be considered to be constant for certain experimental conditions, the hydrogen concentration in the liquid and in the solid phases can vary according to the thermal evolution of the system. This can be quantified as

$$C_{L+S}^{\mathrm{H}} = \frac{\rho_S \cdot (1-g) \cdot C_S^{\mathrm{H}} + \rho_L \cdot g \cdot C_L^{\mathrm{H}}}{\rho_S \cdot (1-g) + \rho_L \cdot g} \tag{21}$$

where ρ_S, $\rho_L$and g are the density of the solid phase, the density of the liquid phase and the volumetric liquid fraction, respectively. The hydrogen concentration in the liquid, C_L^{H}, and in the solid, C_S^{H}, can be related through the equilibrium partition ratio, k_{H} of the H–Al–Cu–Si phase diagram shown in Fig. 1c. The equilibrium partition ratio of hydrogen for the Al–H system is 0.069 [24,25]. The mass concentration dissolved in the liquid phase, C_L^{H}, can be calculated by the equilibrium constant, K_{eq}, of the diatomic gaseous reaction. By considering that the solubility of the diatomic gas in a pure liquid metal obey the Sievert law, we have

$$K_{eq} = \frac{C_L^{\mathrm{H}}}{\sqrt{P_{\mathrm{H}_{2(g)}}}} \tag{22}$$

and the equilibrium constant is defined in terms of the hydrogen solubility as

$$K_{eq} = K_0 \cdot S \tag{23}$$

where K_0 is equal to 2.822×10^{-7} [23] and the solubility of hydrogen can be obtained through the application of *Van't Hoff* equation [24], whose parameters A and B are functions of the local mass concentration of solute and are those used by Boeira et al. [21,22].

Once the barrier imposed by the nucleation condition, given by Eq. (20), is overcome the growth of pores in the mushy zone occurs. It can be quantified by a mass balance analogous to that given by Eq. (21), nevertheless, it takes into account the gas volumetric fraction in the system. For cases where no macrosegregation of hydrogen is considered, we have,

$$\frac{\rho_S \cdot g_S \cdot C_S^H + \rho_L \cdot g_L \cdot C_L^H + \rho_G \cdot g_G \cdot C_G^H}{\rho_S \cdot g_S + \rho_L \cdot g_L + \rho_G \cdot g_G} = C_0^H \quad (24)$$

Consequently, mass, volumetric fractions and the thermophysical properties of the alloy consider the gas fraction according to Eqs. (11)–(14) and (16). The density of the gas can be obtained from the ideal gas equation of state or by a more accurate equation of state similar to that proposed by Peng–Robinson [26].

The pressure of the gas phase results from the association between the local pressure (metalostatic + dynamic pressure) in the mushy zone and an additional pressure imposed by the surface tension:

$$P_G = P + \frac{2 \cdot \sigma_{LG}}{r} \quad (25)$$

σ_{LG} is the surface tension between the gas and the liquid phase, which according to Poirier et al. [24] can be calculated as a function of copper concentration in the liquid by

$$\sigma_{LG} = 0.868 + 0.721 \times 10^{-3} \cdot C_L + 1.29 \times 10^{-5} C_L^2 \quad (26)$$

It is assumed that the pore continues to grow after its nucleation until the solidification is complete. The following linear correlation between the radius of the pore and the volume fraction of the liquid phase is established

$$r = r_0 + (r_{max.} - r_0)\frac{g_L^0 - g_L}{g_L^0} \quad (27)$$

where r_0, $r_{max.}$ and g_L^0 are, the pore nucleation radius, the maximum radius that the pore reaches when local solidification is complete and the volume fraction of the liquid phase when the gas pore first appears, respectively.

To model the formation and evolution of porosity, it was assumed absence of hydrogen macrosegregation. In this way, the hydrogen initially dissolved in the melt is redistributed into the liquid phase and it can be dissolved in the melt until the solidification is complete, or it can combine itself to form molecular hydrogen. It may form gas bubbles in the melt which can grow until the end of solidification.

3. Experimental procedure

The casting assembly used in the directional solidification experiments has been detailed in previous articles [27,28]. The experimental setup consists of a water-cooled mold with heat being extracted from the bottom, promoting a vertical upward directional solidification. The stainless steel mold had an internal diameter of 50 mm, a height of 110 mm and a wall thickness of 3 mm. Experiments were performed with an Al–6 wt%Cu–1 wt%Si alloy, under thermally and solutally stable solidification conditions. The thermophysical properties of this alloy are based on values reported previously for thermal conductivities [18] and on the ThermoCalc software databases for heats of transformation, partition coefficients, specific heats and diffusion coefficients. These data are summarized in Table 1. Continuous temperature measurements in the casting were monitored during solidification via the output of a bank of fine type K thermocouples sheathed in 1.6 mm OD stainless

Table 1
Thermophysical properties of the Al–6 wt%Cu–1 wt%Si alloy used in the numerical simulation.

Properties	Units	Al–6 wt%Cu–1 wt%Si
Liquidus temperature, T_L	°C	638
Initial eutectic temperature, T_{EI}	°C	530.2
Final eutectic temperature, T_{EE}	°C	527.6
Silicon transformation temperature, T_{Si}	°C	513.2
Fusion temperature, T_F	°C	660
Thermal conductivity (solid), k_S	$W\,m^{-1}\,K^{-1}$	180
Thermal conductivity (liquid), k_L	$W\,m^{-1}\,K^{-1}$	87.9
Thermal conductivity (gas), k_L	$W\,m^{-1}\,K^{-1}$	$f(T)$
Density (solid), ρ_S	$kg\,m^{-3}$	2713.4
Density (liquid), ρ_L	$kg\,m^{-3}$	2529.5
Specific heat (solid), c_{PS}	$J\,kg^{-1}\,K^{-1}$	1063
Specific heat (liquid), c_{PL}	$J\,kg^{-1}\,K^{-1}$	1125
Specific heat (gas), c_{Pg}	$J\,kg^{-1}\,K^{-1}$	$f(T)$
Latent heat of fusion, ΔH_1 at $638 \le T < 530.25$ °C	$J\,kg^{-1}$	289,600
Latent heat of fusion, ΔH_2 at $530.25 \le T < 527.54$ °C	$J\,kg^{-1}$	15,800
Latent heat of fusion, ΔH_{eut} at $T = 527.55$ °C	$J\,kg^{-1}$	57,200
Liquidus slope, m_L^{Cu}	$°C\,(wt\%)^{-1}$	3.437
Liquidus slope, m_L^{Si}	$°C\,(wt\%)^{-1}$	7.091
Copper partition coefficient, k_0^{Cu}	–	0.1028
Silicon partition coefficient, k_0^{Si}	–	0.1120
Equilibrium partition coefficient H–Al–Cu–Si, k_H		0.049
Dynamic viscosity of the liquid, μ_L	$kg\,m^{-1}\,s^{-1}$	3×10^{-3}
Thermal expansion coefficient, β_T	K^{-1}	-4.95×10^{-5}
Solutal expansion coefficient, β_C	$(wt\%)^{-1}$	−0.72
Liquid mass-diffusion coefficient of Cu, D_L	$m^2\,s^{-1}$	3.0×10^{-9}
Solid mass-diffusion coefficient of Cu, D_S	$m^2\,s^{-1}$	3.0×10^{-13}
Liquid mass-diffusion coefficient of Si, D_L	$m^2\,s^{-1}$	1.0×10^{-9}
Solid mass-diffusion coefficient of Si, D_S	$m^2\,s^{-1}$	7.0×10^{-12}
Permeability constant, K_0	m^2	6.67×10^{-11}
Global heat-transfer coefficient	$W\,m^{-2}\,K^{-1}$	$14{,}000t^{-0.08}$
Water temperature	°C	20
Nominal concentration of hydrogen, C_0^H	wt%	0.63×10^{-5}
Molar mass of the gas	$kg\,kmol^{-1}$	
Pore nucleation radius, r_0	μm	10
Maximum pore radius, $r_{max.}$	μm	70
External pressure, P_{ext}	Pa	101,324
Universal gas constant	$Pa\,m^3\,kmol^{-1}\,K^{-1}$	8314

steel tubes, and positioned at 5, 10, 15, 30, 50 and 70 mm from the heat-extracting surface at the bottom of the crucible. All thermocouples were connected by coaxial cables to a data logger interfaced with a computer and the temperature data were acquired automatically. The casting was sectioned in the longitudinal direction and the macrostructure was examined. Next, the sample pieces were sectioned into transverse slices and a square central part was cut by the use of a precision saw (Buehler Isomet 4000 with a 0.3 mm thick diamond disk) into pieces of approximately 1.0 mm. Subsequently, the segregation samples were investigated by using a Rigaku Rix 3100 X-ray fluorescence spectrometer to estimate its average concentration through an area of 100 mm^2 probe (probe effective area or the so-called "mask radiated area"). The same sample is rearranged in the mask in order to permit a total of 10 readings of composition at different positions to be obtained. The final results are presented as average local concentrations with the corresponding standard deviation represented by error bars.

The determination of the quantity of pores was based on the pyknometry procedure proposed by McClain et al. [29]. Six different measurements were undertaken for each position along the casting length, with average values and the corresponding standard deviations representing the experimental volumetric fraction of pores. Pyknometry techniques are less time consuming than image analysis techniques and are much less affected by the randomness of the porosity location in the sample [30]. Firstly, the ASMT B 311-93 (Reapproved, 2002) standard was applied in order to determine the apparent density of all the samples as a function of distance from the chill. Secondly, the fraction of pores as a function of the theoretical (ρ_{th}) and apparent (ρ_{ap}) densities was determined. The last step was to provide the theoretical local density for each sample position, based on the experimental macrosegregation profile, by using the following equation:

$$\%\ \text{Pores} = \frac{\rho_{th} - \rho_{ap}}{\rho_{th}} \quad (28)$$

This equation depends not only on the local solute concentration but also on the number of phases involved, their composition and their respective fractions. The phases involved and their volumetric fractions for certain level of local concentration (position dependent) are provided by ThermoCalc® (TCAPI5 interface) using Scheil's model. This procedure is necessary in order to avoid a negative volumetric fraction of pores as previously reported in the literature [31].

4. Results and discussion

Fig. 3a shows the resulting macrostructure of an Al–6 wt%Cu–1 wt%Si alloy casting after upward directional solidification in the vertical water-cooled mold. Fig. 3b exhibits the corresponding experimental solute distribution along the casting length. It is important to remark that a solute profile corresponding to the Fe distribution along the casting has also been included in Fig. 3b. The commercially pure grade aluminum used in this work to prepare the ternary Al–Cu–Si alloy contains approximately 0.08 wt%Fe. This Fe nominal concentration is constant along the casting length except for regions close to the casting cooled surface, where a considerably increase in Fe was noticed (1.02 ± 0.26 wt%Fe), as shown in Fig. 3b. This increase in Fe content was provoked by a diffusive flux of iron from a SAE 1020 steel sheet which physically separates the metal from the cooling fluid in the solidification apparatus. This higher Fe concentration at the regions close to the casting surface will affect the solidification path and the porosity formation, and will be discussed later in this section.

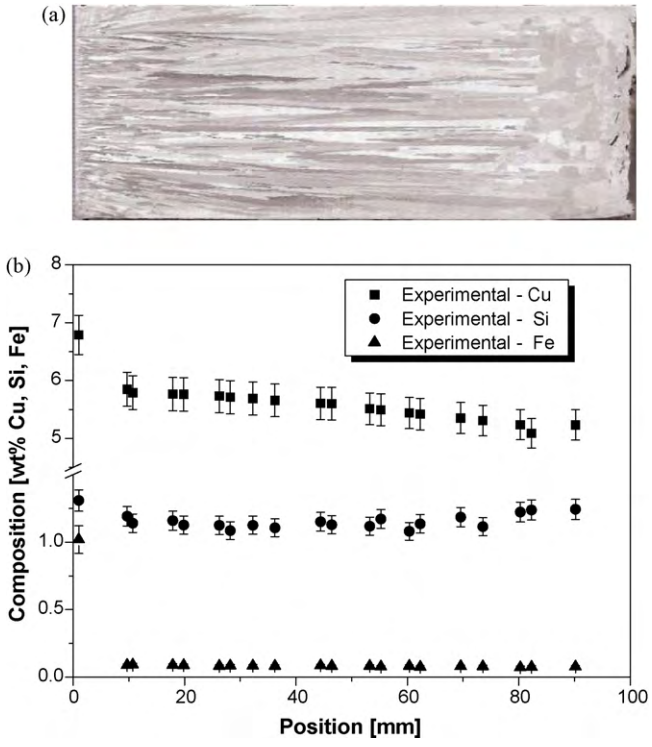

Fig. 3. (a) Casting macrostructure and (b) corresponding experimental composition distribution along the casting length.

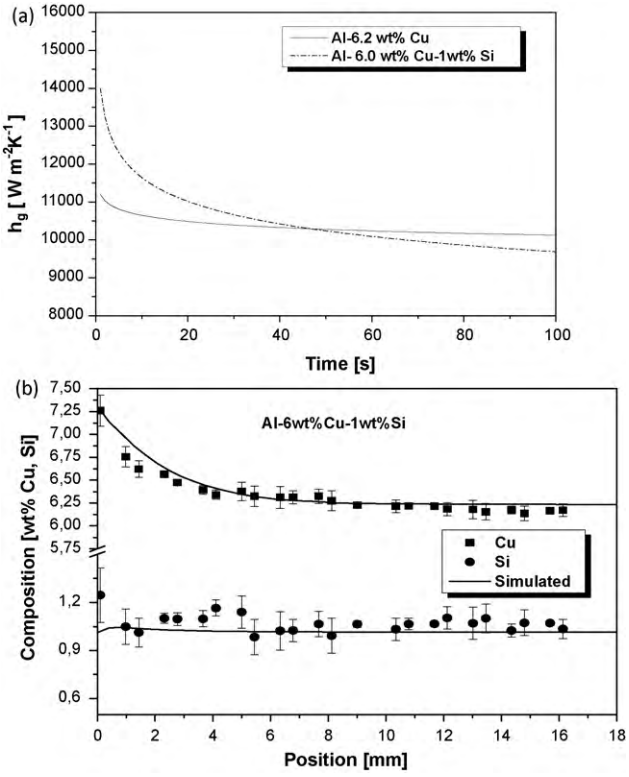

Fig. 4. (a) Comparison of h_g profiles for an Al–6.2 wt%Cu alloy and an Al–6 wt%Cu–1 wt%Si alloy. (b) Detail of experimental and simulated Cu and Si profiles corresponding to positions close to the casting surface highlighting the Cu inverse segregation.

Fig. 4a shows the time dependence of the overall metal/coolant heat-transfer coefficient, h_g, as a function of time, for the ternary alloy examined in the present study ($h_g = 14{,}000t^{-0.08}$ W m^{-2} K^{-1}) and for an Al–6.2 wt%Cu ($h_g = 11200t^{-0.022}$ W m^{-2} K^{-1}) which was solidified in a previous investigation under similar conditions in the same solidification apparatus [22]. It can be seen that the incorporation of 1%Si with respect to the binary Al–6.2 wt%Cu alloy composition has permitted a significantly higher h_g profile to be obtained, mainly at the beginning of solidification of the Al–Cu–Si alloy. Higher heat-transfer coefficient tends to decrease the severity of inverse segregation in binary Al–Cu alloys [22]. The macrosegregation profile for the Al–6 wt%Cu–1 wt%Si alloy casting [19] is shown in Fig. 4b where experimental measurements are compared with numerical results. A comparison between the inverse Cu profile shown in Fig. 4b with that obtained in the previous study with the Al–6.2 wt%Cu [22], i.e., alloys with similar Cu concentrations, permits to demonstrate that the higher initial h_g values of the ternary alloy associated with differences in the solidification

path have induced higher Cu concentrations at the ternary alloy casting surface. It can also be seen in Fig. 4b that the model computes the inverse (Cu) solute concentration profile, and a very good agreement with experiment is observed. No macrosegregation is observed with respect the silicon distribution along the length of the directionally solidified casting, except for a single point of positive segregation, probably associated with both the formation of the mushy zone length and the backward flow induced by solidification contraction.

Once the alloy composition is specified, the only means remaining to exert control on microstructural parameters is in modifying the thermal variables during solidification (solidification velocity, cooling rate and thermal gradient). The direction of solidification with respect to the gravity vector has also to be considered because gravity driven segregation can also be produced [32]. These solidification thermal variables affect significantly the formation of dendrite spacings during freezing, which strongly affect the development of porosity. Hence, accurate porosity data obtained during transient directional solidification are fundamental to understand the coupling phenomena among the solidification thermal variables, microstructure features and porosity formation. Fig. 5 shows typical transverse microstructures obtained during the directional solidification of an Al–6 wt%Cu–1 wt%Si alloy, for different cooling rates. It can be seen that the primary dendritic spacing increases as the cooling rate decreases, i.e., from the bottom to the top of the unidirectionally solidified casting. The primary dendritic spacing evolution with the cooling rate is shown in Fig. 6 compared with the corresponding values for binary hypoeutectic Al–Cu alloys [33].

The use of anisotropic permeability channels have proved to provide more accurate simulated results for pores evolution along the casting length of binary Al–Cu alloys [22]. The simulations performed in the present study are based on permeability coefficients which are function of the primary dendritic arm spacing. The experimental dendrite growth laws shown in Fig. 6 were used to determine the permeability coefficients. Fig. 7 shows the evolution of the theoretical density (based on the macrosegregation profile of Fig. 4b and on the corresponding apparent densities). The resulting simulations of pore volumetric fractions along the casting length compared with the corresponding experimental results are shown in Fig. 8. It can be seen that for both alloys the numerically simulated trend is in good conformity with the experimental scatter. The volumetric fractions of pores depict linear ascending trends from the bottom to the top of the casting for both alloys. However, the datasets for the Al–6%Cu–1%Si and Al–6.2%Cu alloys show points of inflection. These oscillations observed in the porosity experimental data can probably be associated with the occurrence of burst feeding, i.e., the strength of the mushy zone is exceeded by the stresses caused by continued solidification shrinkage. The numerical simulation determines porosity to be a linear function of position along the casting length because the numerical model does not take into account the effect of burst feeding.

The results of Fig. 8 show that the addition of 1 wt%Si to the composition of an Al–6 wt%Cu alloy increases significantly the volume of pores. It can also be seen an abnormal volumetric fraction of pores close to the ternary alloy casting surface, which is caused by the corresponding higher Fe concentration shown in Fig. 3b.

Iron and silicon alone do not seem to have any special contribution to porosity. However, they form intermetallics whose morphology affects feeding [13]. It has been reported in the literature that porosity increases with iron content because Al_5FeSi platelets (β phase) block the interdendritic channels, impeding feeding and leading to micro-shrinkage porosity [34,35]. The nominal content of iron (0.08 wt%Fe) in the ternary alloy used in the present study would form only small amounts of Al_7Cu_2Fe phase along the ingot length during transient solidification. Then, for a first sample situated close to the cooled surface (<7 mm) having

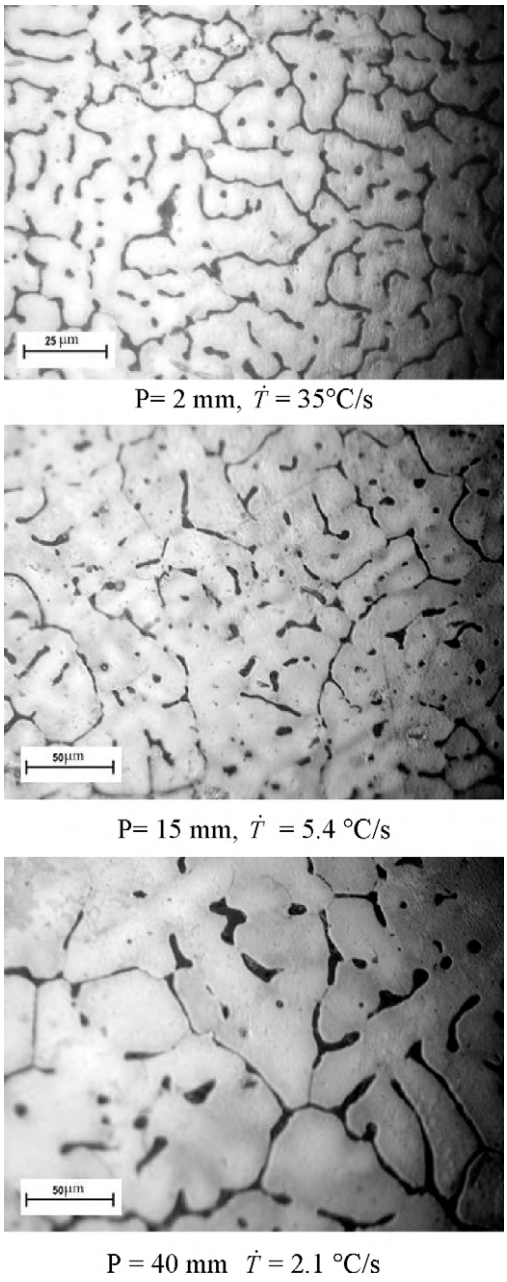

Fig. 5. Typical transverse microstructures of the directionally solidified casting. *P* is the position from the casting cooled surface and $\dot{T}$ is the cooling rate.

about 1 wt%Fe, according to Fig. 9a, we have the following solidification sequence:

(i) primary aluminum dendrites (FCC_A1) up to $f_S = 0.36$, followed by the Al_3Fe compound which is formed until $f_S = 0.53$ is reached;
(ii) after this, Al_5FeSi_α is formed until $f_S = 71.4$;
(iii) from $f_S = 71.4$ to 81.5, Al_7Cu_2Fe is formed;
(iv) between $f_S = 81.5$ and $f_S = 83.4$, the Si phase precipitates;
(v) finally, from $f_S = 83.4$ to $f_S = 1$, the ternary eutectic reactions take place.

For positions farther than 7 mm from the casting surface (as reference, a sample positioned at 16 mm from the cooled surface has been considered), the solidification sequence, shown in Fig. 9b can be summarized as follows:

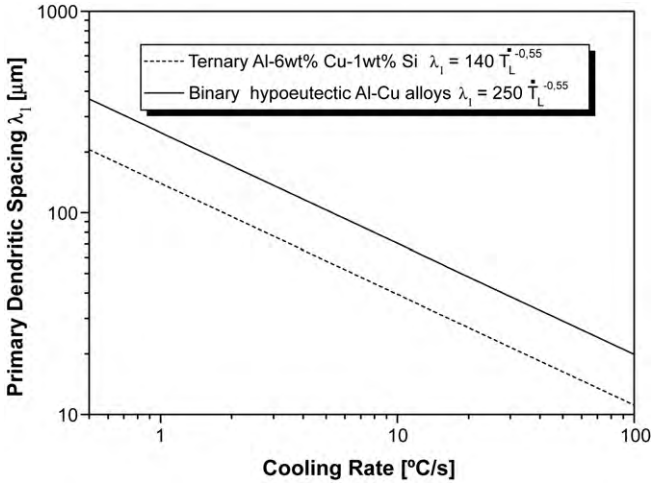

Fig. 6. Experimental evolution of primary dendritic arm spacing with cooling rate.

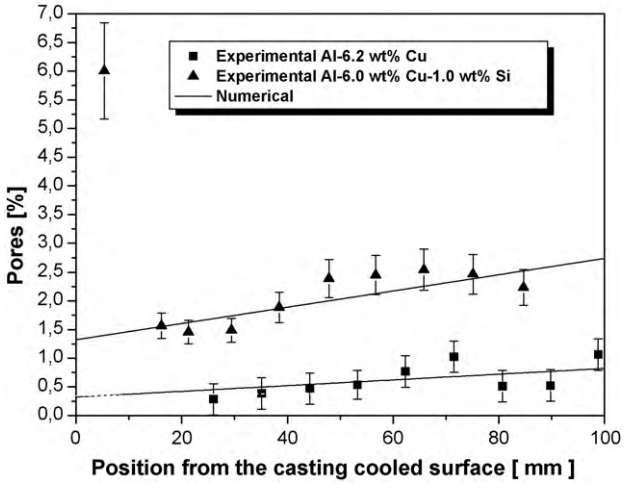

Fig. 8. Comparison between results for a binary Al–6.2 wt%Cu alloy [22] and a ternary Al–6 wt%Cu–1 wt%Si alloy: numerically calculated and experimental micro-porosity scatter.

(i) primary aluminum dendrites (FCC_A1) solidify until the solid fraction reaches $f_S = 0.795$;
(ii) from $f_S = 0.795$ to 0.836, Al_7Cu_2Fe is formed;
(iii) between $f_S = 83.6$ and $f_S = 84.2$, the Si phase precipitates;
(iv) finally, from $f_S = 84.2$ to $f_S = 1$, the ternary eutectic phase is formed.

Dinnis et al. [13] stated that the effect of iron on porosity levels in hypoeutectic Al–Si foundry alloys is complex due a relation between copper and iron content. They concluded that the existing theories were incomplete and inadequate to explain iron addition-porosity formation. They demonstrated that increasing

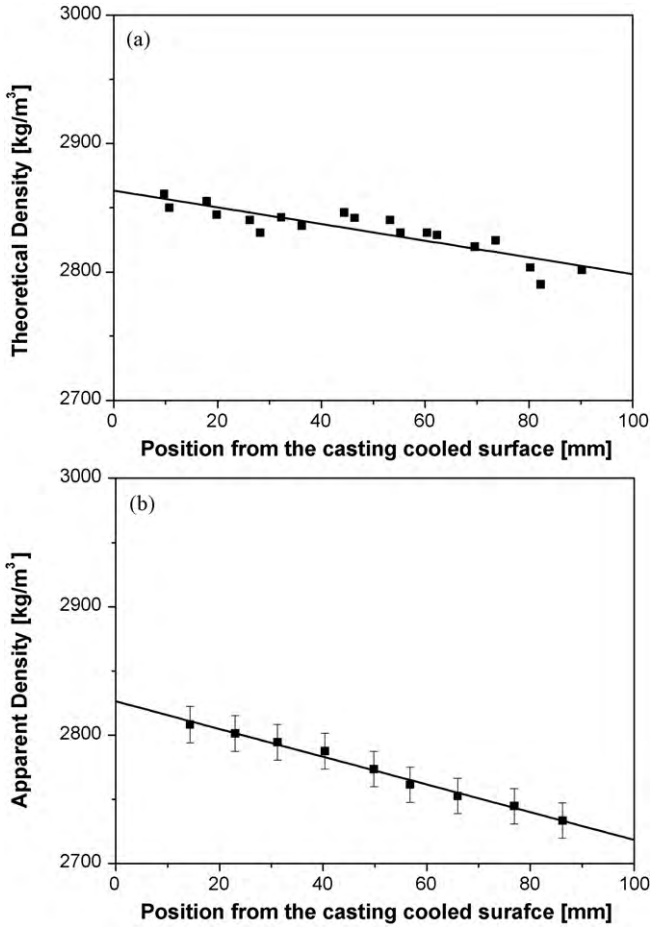

Fig. 7. (a) Theoretical density calculated as a function of local experimental chemical composition and (b) apparent density experimentally determined.

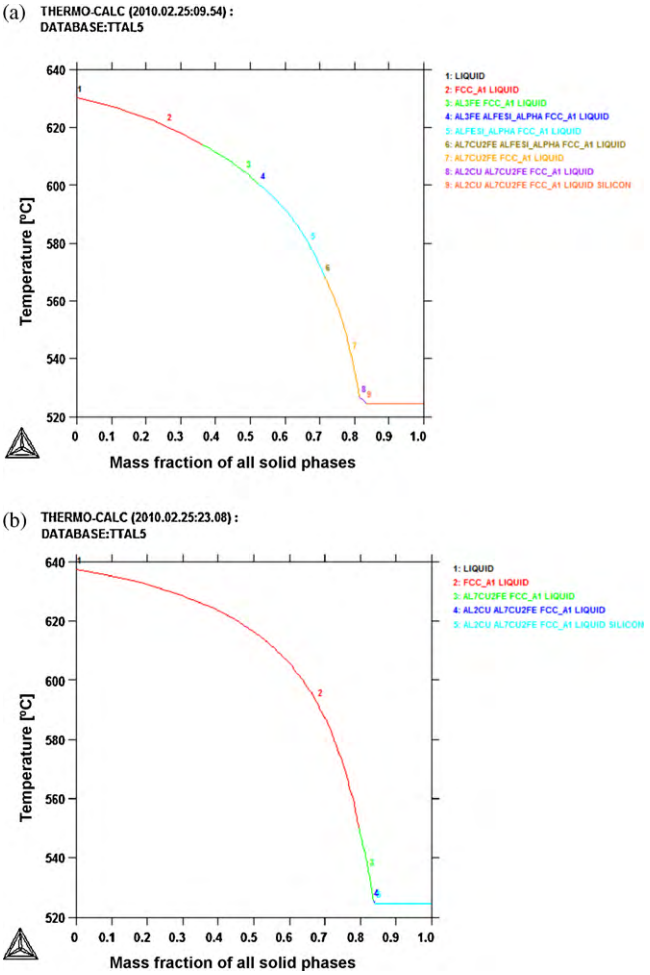

Fig. 9. Solidification path (ThermoCalc TTAL5): (a) for regions close to the casting cooled surface and (b) for positions > 7 mm from the casting cooled surface.

iron concentrations have been shown to increase porosity in a wide range of Al–Si–Mg–Cu alloys. However, the effect of iron on porosity changes as the silicon and copper concentrations of the alloys change. Increasing iron concentrations also lead to a refinement in the size of the regions of Al_2Cu.

5. Conclusions

The macrosegregation evolution and microporosity formation in a ternary Al–6 wt%Cu–1 wt%Si alloy were evaluated by a numerical modelling approach, considering secondary phases, local composition, and consequently local density. Unidirectional solidification experiments were carried out under conditions of transient metal/mold heat-transfer coefficient (h_g) in order to provide experimental results to validate the model predictions. A very good agreement has been observed between theoretical predictions and experimental results. Macrosegregation is absent for the silicon content, along the length of the casting, but a comparison between the present experimental inverse Cu profile and that obtained in a previous study with an Al–Cu alloy with similar Cu concentration, demonstrated that the higher initial h_g values of the ternary alloy associated with differences in the solidification path, have induced higher Cu concentrations at the ternary alloy casting surface. The volumetric fractions of pores depict an ascending linear trend from the bottom to the top of the casting. The numerically simulated trend is in good conformity with the experimental scatter, except for points of inflection which were observed in the porosity experimental data and that can probably be associated with the occurrence of burst feeding, not considered by the numerical model. A significant increase in the fraction of pores was noticed when 1 wt%Si was added to the composition of an Al–6 wt%Cu alloy. It was shown that a higher Fe concentration at the regions close to the casting surface caused by a diffusive flux of iron from the steel chill mold increased remarkably the volume of pores at the casting surface.

Acknowledgements

The authors acknowledge the financial support provided by FAPESP (The Scientific Research Foundation of the State of São Paulo, FAEPEX-UNICAMP), FAPERJ (The Scientific Research Foundation of the State of Rio de Janeiro, Grant Number E-26/110.664/2009), CAPES and CNPq (The Brazilian Research Council).

References

[1] J.P. Weiler, W.T. Wood, Mater. Sci. Eng. A 527 (2009) 32–37.
[2] J.-Y. Buffiere, S. Savelli, P.H. Jouneau, E. Maire, R. Fougeres, Mater. Sci. Eng. A 316 (2001) 115–126.
[3] H.S. Whitesell, R.A. Overfelt, Mater. Sci. Eng. A 318 (2001) 264–276.
[4] A. Shafyei, S.H. Mousavi Anijdan, A. Bahrami, Mater. Sci. Eng. A 431 (2006) 206–210.
[5] K. Li, E. Chang, Acta Mater. 52 (2004) 219–231.
[6] T.S. Piwonka, S. Kuyucak, K.G. Davis, AFS Trans. 113 (2002) 1257–1271.
[7] J. Campbell, Castings, Butterworth-Heinemann, Oxford, Great Britain, 2003.
[8] A.K. Dahle, L. Arnberg, D. Apelian, AFS Trans. 160 (1997) 963–969.
[9] M. Dash, M. Makhlouf, J. Light Met. 1 (2001) 251–265.
[10] A.K. Dahle, L. Arnberg, Acta Mater. 45 (1997) 547–559.
[11] R. Fuoco, E.R. Correa, M.D.A. Bastos, AFS Trans. 106 (1998) 401–409.
[12] L. Arnberg, AFS Trans. 103 (1995) 753–760.
[13] C.M. Dinnis, J.A. Taylor, A.K. Dahle, Mater. Sci. Eng. A 425 (2006) 286–296.
[14] P.D. Lee, R.C. Chirazi, R.C. Atwood, W. Wang, Acta Mater. 51 (2003) 5447–5466.
[15] V.R. Voller, Can. Metall. Quart. 37 (1998) 169–177.
[16] C.R. Swaminathan, V.R. Voller, Int. J. Heat Mass Transf. 40 (1997) 2859–2868.
[17] C.Y. Wang, C. Beckermann, Metall. Trans. A 24 (1993) 2787–2802.
[18] I.L. Ferreira, B. Nestler, A. Garcia, Scripta Mater. 50 (2004) 407–411.
[19] I.L. Ferreira, D.J. Moutinho, L.G. Gomes, O.L. Rocha, A. Garcia, Philos. Mag. Lett. 89 (2009) 769–777.
[20] V.D. Tsoukalas, Mater. Des. 29 (2008) 2027–2033.
[21] A.P. Boeira, I.L. Ferreira, A. Garcia, Mater. Sci. Eng. A 435–436 (2006) 150–157.
[22] A.P. Boeira, I.L. Ferreira, A. Garcia, Mater. Des. 30 (2009) 2090–2098.
[23] A.V. Kuznetsov, M. Xiong, Int. Commun. Heat Mass Transf. 29 (2002) 25–34.
[24] D.R. Poirier, K. Yeum, A.L. Maples, Metall. Mater. Trans. A 18 (1987) 1979–1987.
[25] J. Huang, T. Mori, J.G. Conley, Metall. Mater. Trans. B 29 (1998) 1249–1257.
[26] D.Y. Peng, D.B. Robinson, Ind. Chem. Fundam. 15 (1976) 59–64.
[27] P.R. Goulart, K.S. Cruz, J.E. Spinelli, I.L. Ferreira, N. Cheung, A. Garcia, J. Alloys Compd. 470 (2009) 589–599.
[28] A.P. Silva, J.E. Spinelli, A. Garcia, J. Alloys Compd. 475 (2009) 347–351.
[29] S.T. McClain, A.S. McClain, J.T. Berry, AFS Trans. 109 (2001) 321–332.
[30] S.T. McClain, A.S. McClain, J.T. Berry, AFS Trans. 108 (2000) 185–189.
[31] V.R. Voller, S.A. Sundarraj, Int. J. Heat Mass Transf. 38 (1995) 1009–1018.
[32] I.L. Ferreira, J.E. Spinelli, A. Garcia, J. Alloys Compd. 475 (2009) 396–400.
[33] O.L. Rocha, C.A. Siqueira, A. Garcia, Metall. Mater. Trans. A 34 (2003) 995–1006.
[34] J.A. Taylor, G.B. Schaffer, D.H. StJohn, Metall. Mater. Trans. A 30 (1999) 1643–1650.
[35] J.A. Taylor, G.B. Schaffer, D.H. StJohn, Metall. Mater. Trans. A 30 (1999) 1657–1662.